

Transformation Superplasticity of Iron and Fe/TiC Metal Matrix Composites

PETER ZWIGL and DAVID C. DUNAND

Unreinforced iron was thermally cycled around the α/γ phase field under an externally applied uniaxial tensile stress, resulting in strain increments which could be accumulated, upon repeated cycling, to a total strain of 450 pct without failure. In agreement with existing theory attributing transformation superplasticity to the biasing of the internal allotropic strains by the external stress, the measured strain increments were proportional to the applied stress at small stresses. However, for applied stresses higher than the nominal yield stress, strain increments increased nonlinearly with stress, as a result of strain hardening due to dissolved carbon and iron oxide dispersoids. Also, the effects of transient primary creep and ratchetting on the superplastic strain increment values were examined. Finally, partial cycling within the α/γ phase field indicated an asymmetry in the superplastic strain behavior with respect to the temperature cycling range, which is attributed to the different strengths of ferrite and austenite. Transformation superplasticity was demonstrated in iron-matrix composites containing 10 and 20 vol pct TiC particles: strain increments proportional to the applied stress were measured, and a fracture strain of 230 pct was reached for the Fe/10TiC composite. However, the strain increments decreased with increasing TiC content, a result attributed to the slight dissolution of TiC particles within the matrix which raised the matrix yield stress by solid-solution strengthening and by reducing the transformation temperature range.

I. INTRODUCTION

THE addition of reinforcing ceramic particulates to iron or steel leads to composites with improved strength, stiffness, and abrasion resistance. Titanium carbide (TiC) is particularly attractive, because of its high hardness and stiffness, its low density, and its chemical stability with iron-based matrices.^[1,2] However, the low ductility, low toughness, and high hardness of Fe/TiC composites severely limit traditional forming techniques such as bending, stamping, rolling, forging, or machining. Superplastic forming is, thus, an attractive method for fabricating objects with intricate shapes from simple composite sheets or tubes, which can be produced for Fe/TiC by a near-net-shape technique such as casting^[3,4] or powder metallurgy.^[5,6] Microstructural superplasticity is, however, very difficult to achieve in Fe/TiC composites, because these materials are too brittle for the thermomechanical treatment necessary to generate a fine grain size, and because ceramic reinforcement can inhibit grain boundary sliding. An alternative superplastic deformation mechanism not necessitating a fine-grained structure is transformation superplasticity, which relies on internal stresses produced by repeated allotropic transformations.^[7,8]

Plasticity induced by a phase transformation has been extensively studied in unreinforced iron and steels, and can result from two distinct mechanisms: (1) preferential selection by the applied stress of martensite variants with a non-

zero shear,^[9-13] or (2) biasing by the applied stress of isotropic internal stresses due to the volumetric mismatch between allotropic phases during the transformation.^[7,8,14] For the latter mechanism, these internal mismatch stresses are generated at each crossing of the allotropic range, so that strain increments can be accumulated after each cycle, eventually resulting in superplastic elongations (>100 pct).^[15,16,17] Depending on the material properties and the phase transformation homologous temperature, the internal transformation mismatch stresses can be relaxed by time-independent plastic deformation or by creep.^[14] For the former case, Greenwood and Johnson^[14] developed an equation for the uniaxial strain increment $\Delta\varepsilon$, accumulated after a full allotropic transformation, occurring with a superimposed uniaxial biasing tensile stress σ .

$$\Delta\varepsilon = \frac{5}{6} \left| \frac{\Delta V}{V} \right| \frac{\sigma}{\sigma_Y} \quad [1]$$

where $|\Delta V/V|$ is the volume mismatch between the allotropic phases, and σ_Y is the yield stress of the weaker allotropic phase. Equation [1] is valid for small strains only ($\Delta\varepsilon \ll |\Delta V/V|$) and for an ideally plastic material without strain hardening.

While transformation superplasticity has been studied in iron and steels (and many other allotropic metals^[7,8,14]), little is known about this phenomenon in metal matrix composites. Transformation superplasticity was recently demonstrated in allotropic titanium-based composites,^[18,19] where accommodation of internal stresses is by creep, but has never been studied in composites such as Fe/TiC, where accommodation is by time-independent yield.

In the present article, we investigate transformation superplasticity of unreinforced iron and Fe/TiC composites upon thermal cycling about the α/γ -iron phase field and

PETER ZWIGL, Graduate Research Assistant, is with the Department of Materials Science and Engineering, Massachusetts Institute of Technology, Cambridge, MA 02139. DAVID C. DUNAND, Associate Professor, formerly with the Department of Materials Science and Engineering, Massachusetts Institute of Technology, is with the Department of Materials Science and Engineering, Northwestern University, Evanston, IL 60208.

Manuscript submitted June 10, 1997.

Table I. Chemical Compositions

Material	Carbon (Wt Pct)	Other Elements (Wt Pct)	Analysis
Fe (as received)	0.009	0.003N 0.28O	Alfa Aesar, MA
Fe (HIP)	0.012	0.018Si 0.019Mn	Luvak, MA
TiC (as-received)	19.6 ± 0.1		Mass. Materials Research, MA

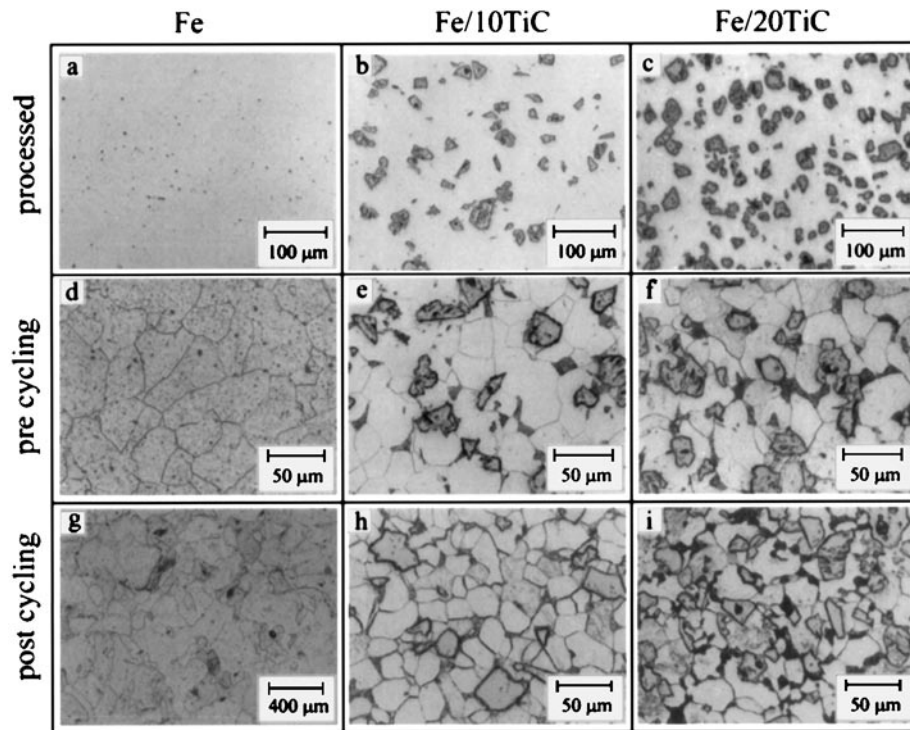


Fig. 1—(a) through (i) Micrographs of iron, Fe/10TiC, and Fe/20TiC samples before thermal cycling (unetched), before thermal cycling (etched), and after thermal cycling (etched).

examine the effects of TiC volume fraction and applied stress, as well as the temperature cycling amplitude and frequency. The superplastic behavior is demonstrated by experiments conducted up to large strains, and special emphasis is put on the link between transformation superplasticity and the thermal and microstructural characteristics of the materials.

II. MATERIALS AND EXPERIMENTAL PROCEDURES

Iron powders with a particle size of 6 to 10 μm and a purity of 99.5 pct (from Alfa Aesar, Ward Hill, MA) were mixed for 12 hours in a V-Blender with 10 and 20 vol pct of 99.5 pct pure TiC powders (from CERAC, Milwaukee, WI). Before blending, the as-received -325 mesh TiC had been suspended in deionized water and filtered through a Buchner filtering funnel with a porosity of 10 to 20 μm to eliminate the fine particles, ensuring a final TiC size distribution between 20 and 45 μm . Both unblended iron powders and blended Fe/TiC powder mixtures were cold-pressed into low-carbon steel pipes (ASM 5050J steel with 25.4-mm outside diameter, 3.2-mm wall thickness, and 228-mm height, welded at both ends with 1018 steel plugs),

degassed under vacuum at an elevated temperature, and compacted by hot isostatic pressing (“HIP”) for 4 hours at 1121 $^{\circ}\text{C}$ under a pressure of 103 MPa (at UltraClad, Andover, MA).

Small samples were tested by differential thermal analysis (DTA) using a PERKIN-ELMER,* Series 7 instrument

*PERKIN-ELMER is a trademark of Perkin-Elmer Physical Electronics, Eden Prairie, MN.

at a rate of $\dot{T} = 10$ K/min under flowing nitrogen, with alumina as reference material. Parallelepiped samples (approximately $12 \times 3 \times 3$ mm) were studied by dilatometry (Netzsch 402 ES) with $\dot{T} = 10$ K/min under flowing argon. Dogbone samples with a gage length of 35 mm and a gage diameter of 6 mm were tested in tension in a custom-designed creep apparatus, allowing the application of small tensile stresses simultaneous to rapid temperature cycling by radiation in an argon atmosphere. Before thermal cycling, the samples were crept isothermally until a steady-state strain rate was reached. The deformation was measured by a linear voltage displacement transducer placed at the cold end of the lower pullrod. Under cycling conditions, the measured deformation included the thermal dilatation of the pullrods and samples and, therefore, did

Table II. Porosity (v) and Density (ρ) for Iron and Fe/TiC MMCs after Cold Pressing, HIP, and Deformation to Strain (e)

Material	After HIP		After Deformation		e (%)
	ρ (g/cm ³)	v (Vol Pct)	ρ (g/cm ³)	v (Vol Pct)	
Fe	7.81	0.2	7.82	0.2	172
Fe/10TiC	7.54	0.0	7.54	0.0	51
Fe/20TiC	7.24	0.1	7.25	0.0	2

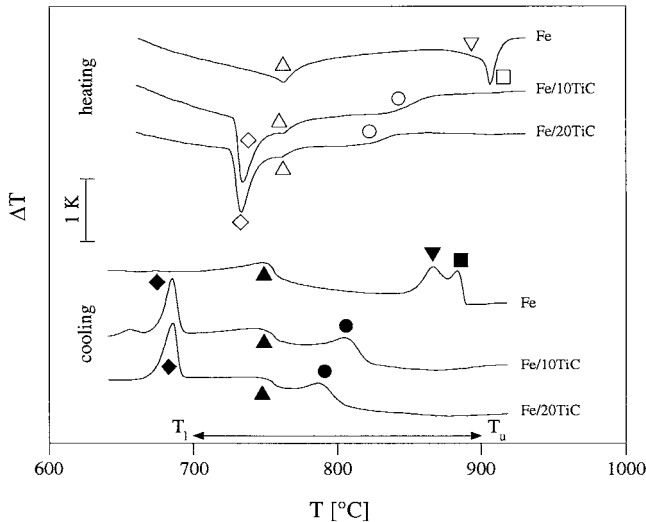


Fig. 2—DTA of iron and Fe/TiC composites with $\dot{T} = 10$ K/min; $\alpha \leftrightarrow \gamma$ transformation \square , \blacksquare ; martensite reactions or $\alpha \leftrightarrow \gamma$ recalescence peak ∇ , \blacktriangledown ; $\alpha + \text{TiC} \leftrightarrow \gamma + \text{TiC}$ transformation \circ , \bullet ; magnetic transition Δ , \blacktriangle ; and $\text{Fe}_3\text{C} + \text{TiC} + \alpha \leftrightarrow \alpha + \gamma + \text{TiC}$ reaction \diamond , \blacklozenge .

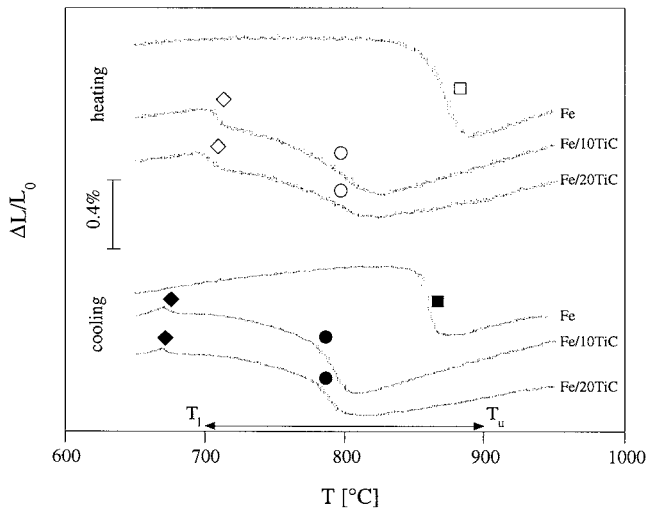


Fig. 3—Dilatometry of iron and Fe/TiC composites with $\dot{T} = 10$ K/min (same symbols as in Fig. 2).

not represent the sample plastic strain. However, the strain measured under isothermal conditions or after a full temperature cycle was only due to the sample plastic deformation. The total plastic strain increment per cycle ($\Delta \epsilon_{\text{tot}}$) was calculated as the average of four to six values, measured after the strain increments had reached steady state, to avoid any primary creep strain contribution. The sample

stress was adjusted manually by periodically applying or removing weights. Standard deviations for stress and strain were below 5 pct. The temperature of the sample was controlled within ± 2 °C by a thermocouple (K type or R type) positioned at the surface of the gage section or the pullhead and independently measured by a second thermocouple located at the sample surface. The latter temperature varied by ± 15 °C between different experiments due to slight variations in sample and/or thermocouple position with respect to the radiant heaters.

Densities were determined by the Archimedes method with distilled water. Metallographic preparation of undeformed and deformed samples was performed by grinding with SiC papers with a 120, 500, 1200, and 2400 mesh; polishing on cloths with 0.3- and 0.05- μm alumina; and etching by swabbing for 20 seconds with a 2 pct Nital solution.

III. RESULTS

A. Materials

Table I gives the chemical analysis of the as-received powders and the HIP iron sample. The measured carbon content of the as-received TiC powders is close to the theoretical concentration for a TiC powder with the highest possible carbon content (19.3 wt pct C or 48.8 at. pct C),^[20] indicating that the as-received TiC powder was as close to stoichiometry as thermodynamically possible. Slight carbon contamination of the iron billet (and, thus, most probably, of the composite billets) occurred during HIP by diffusion of carbon and other alloying elements from the steel can.

Assuming that the oxygen present in the iron matrix exists in the form of iron oxides (Fe_3O_4 or Fe_2O_3), and using density values given in Reference 21, the theoretical density of the unreinforced matrix is determined as $\rho_{\text{matrix}} = 7.83$ g/cm³, indicating that the iron sample is 99.8 pct dense (Table II). With the theoretical density of TiC as $\rho_{\text{TiC}} = 4.92$ g/cm³,^[22] similarly low porosities are calculated for the composites after HIP and after deformation (Table II).

Figures 1(a) through (c) and Figures 1(d) through (f) show micrographs of the HIP samples in unetched and etched conditions, respectively. The iron sample exhibits both oxides and pores (Figure 1(a)). The unetched micrographs of the composites (Figures 1(b) and (c)) show that the TiC particles are well distributed within a dense matrix. However, etching reveals other precipitates at the grain boundaries (Figures 1(e) and (f)). The grain size of the iron samples, as determined by the linear intercept method, increased from 34 ± 4 μm after HIP (Figure 1(d)) to 62 ± 8 μm at the pullhead and 340 ± 70 μm (Figure 1(g)) at the gage section after thermal cycling under stress. On the other hand, the grain size of the Fe/10TiC composite remained stable, with values of 30 ± 3 μm after hot isostatic pressing (Figure 1(e)) and 23 ± 4 μm after thermal cycling (Figure 1(h)). Similar grain sizes were obtained for the Fe/20TiC composite (Figures 1(f) and (i)). Furthermore, the same grain sizes were found in the sample heads and gage section of the deformed composites.

The DTA curve (Figure 2) and dilatometric curve (Figure 3) exhibit multiple peaks corresponding to phase transformation and precipitation, labeled in both figures with the same symbols.

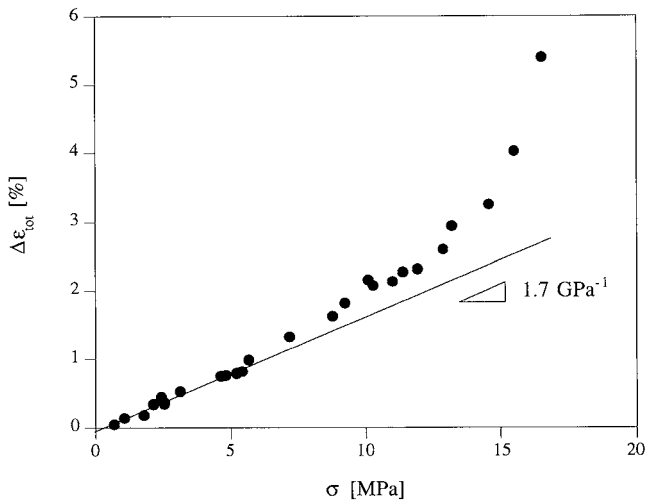


Fig. 4—Strain increment per cycle as a function of the applied stress for iron ($T_l = 700^\circ\text{C}$, $T_u = 900^\circ\text{C}$, and $\nu = 6$ to 10 h^{-1}).

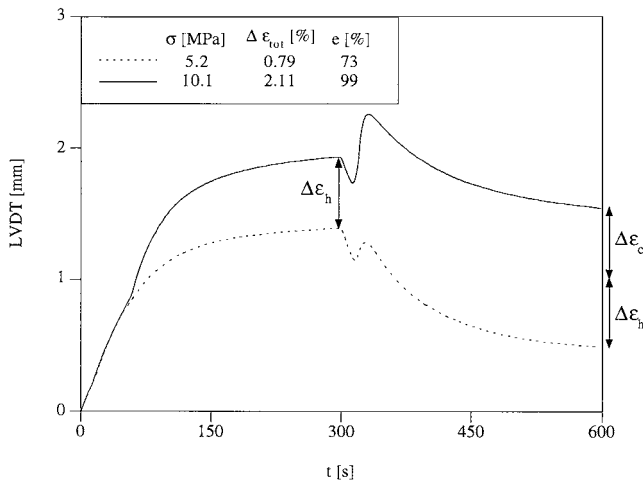


Fig. 5—Total deformation of two cycles with two different stress levels for iron.

B. Thermal Cycling of Iron

Figure 4 shows the total strain increment ($\Delta\epsilon_{\text{tot}}$) as a function of the applied stress (σ) for complete square-wave cycles between $T_l = 700^\circ\text{C}$ and $T_u = 900^\circ\text{C}$, with heating and cooling rates in the range of $\dot{T} = 100$ to 200 K/min and with cycling frequencies in the range of $\nu = 6$ to 15 h^{-1} . The data are insensitive to the cycle frequency within the experimental range used, as seen from the continuity of the results in Figure 4. The strain increment increases linearly with an applied stress up to $\sigma \approx 6\text{ MPa}$, and becomes nonlinear for higher stresses. Within the linear range, a slope of $(d\Delta\epsilon_{\text{tot}})/d\sigma = 1.7\text{ GPa}^{-1}$ and an intercept of $\Delta\epsilon_{\text{tot}} = -0.05\text{ pct}$ for zero applied stress are found. Isothermal creep measurements were performed at the upper and lower cycling temperatures before and after thermal cycling, giving stress exponents between 1 and 2. For all experiments, it was found that the isothermal strain rates caused by creep were negligible compared to the cycling strain rates. For example, at the upper cycling temperature, the iron sample crept at $\dot{\epsilon} = 3.3 \cdot 10^{-7}\text{ s}^{-1}$ for a stress of $\sigma = 4.2\text{ MPa}$, much more slowly than under cycling conditions with $\nu = 6\text{ h}^{-1}$ where the average strain rate was $d(\Delta\epsilon_{\text{tot}})/dt = 1.3 \cdot$

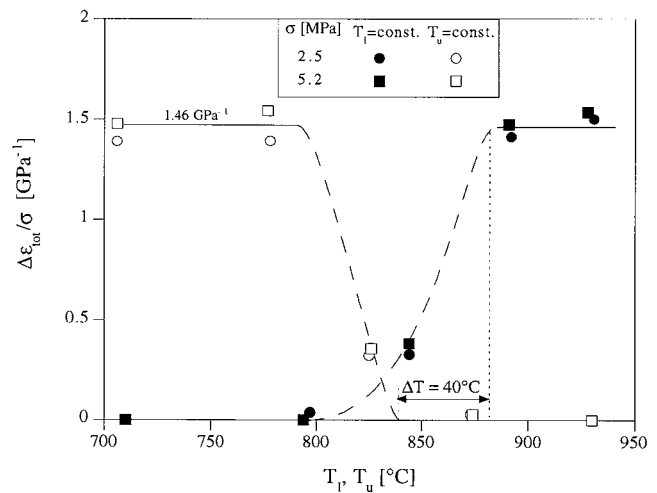


Fig. 6—Stress-normalized strain increment for iron as a function of the upper temperature for cycles with a constant lower temperature $T_l = 710^\circ\text{C}$ and as a function of the lower temperature for cycles with a constant upper temperature $T_u = 930^\circ\text{C}$ ($\nu = 10\text{ h}^{-1}$, $\sigma = 2.5\text{ MPa}$ and 5.2 MPa).

10^{-5} s^{-1} for $\sigma = 4.6\text{ MPa}$. For a higher applied stress of $\sigma = 10.3\text{ MPa}$, the isothermal creep strain rate $\dot{\epsilon} = 2 \cdot 10^{-6}\text{ s}^{-1}$ was still much smaller than the average cycle strain rate of $d(\Delta\epsilon_{\text{tot}})/dt = 8.8 \cdot 10^{-5}\text{ s}^{-1}$ (for a frequency of $\nu = 15\text{ h}^{-1}$). In several instances, the isothermal creep rates dropped after thermal cycling by factors of between 2 and 5. Creep rates at the lower cycling temperature were not detectable.

Figure 5 shows two examples of the displacement measured over a full cycle for applied stresses of 5.2 and 10.1 MPa. For these cycling conditions and sample geometry, the total strain increment per cycle is composed of equal contributions on heating and on cooling. Also visible in Figure 5 are discontinuities on heating and cooling corresponding to the phase transformations. During heating, the sample superplastic strain and the thermal expansion of the load-train give contributions in the same direction, causing a discontinuity at the phase transformation temperature, whereas during cooling, the thermal contraction of the load-train opposes the sample elongation due to the superplastic strain increment, leading to a distinct phase transformation peak. The effect of the upper- and lower-temperature-cycle amplitude on the stress-normalized strain increment ($\Delta\epsilon_{\text{tot}}/\sigma$) is shown in Figure 6 for two stress levels. While keeping the lower temperature constant at $T_l = 710^\circ\text{C}$, the upper cycle temperature was gradually increased to $T_u = 930^\circ\text{C}$; the symmetric experiments (constant upper temperature $T_u = 930^\circ\text{C}$ and variable lower temperature T_l) were also performed.

Finally, Figure 7 shows an unfractured iron sample deformed to an engineering strain of $e = 454\text{ pct}$ after 242 cycles ($T_l = 700^\circ\text{C}$, $T_u = 900^\circ\text{C}$, and $\nu = 15\text{ h}^{-1}$) under an applied stress of $\sigma = 7.2 \pm 0.2\text{ MPa}$ for the first 140 cycles and a stress of $\sigma = 4.9 \pm 0.3\text{ MPa}$ for the last 102 cycles. Figure 8 shows, for that sample, the stress-normalized strain increment per cycle ($\Delta\epsilon_{\text{tot}}/\sigma$) as a function of the number of cycles (i). The discontinuities are due to adjustments of the load to maintain an approximately constant stress. Before cycling, the sample was not crept isothermally, but was thermally cycled under a small stress of 0.4 MPa, which resulted in very small negative strain in-

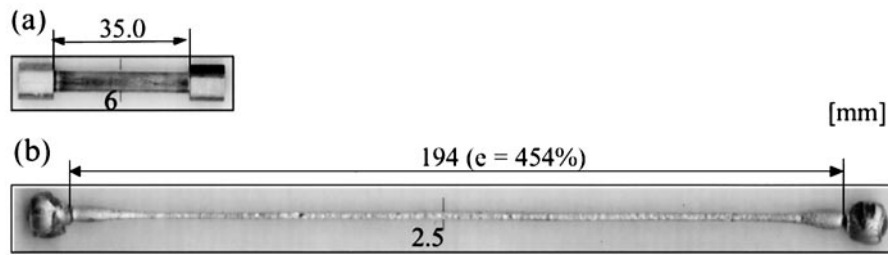


Fig. 7—Iron sample (a) undeformed and (b) deformed at constant stress for 242 cycles ($\sigma = 7.2$ for 140 cycles and $\sigma = 4.9$ for 102 cycles) between 700 °C and 900 °C ($\nu = 15 \text{ h}^{-1}$).

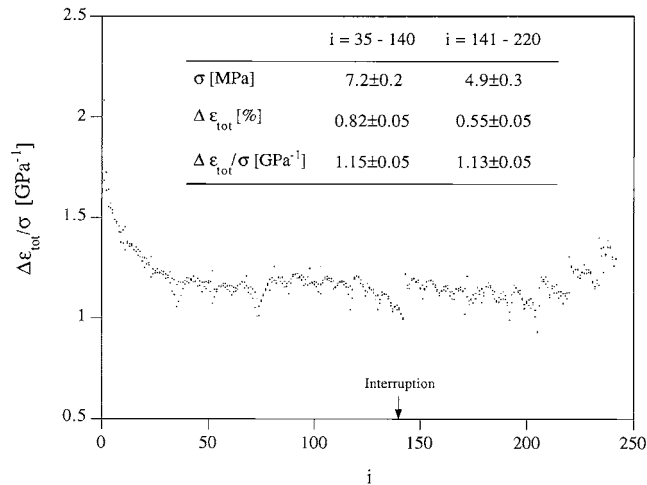


Fig. 8—Stress-normalized strain increment as a function of the number of cycles for iron; no isothermal precreep prior to thermal cycling ($T_i = 700$ °C, $T_u = 900$ °C, and $\nu = 15 \text{ h}^{-1}$).

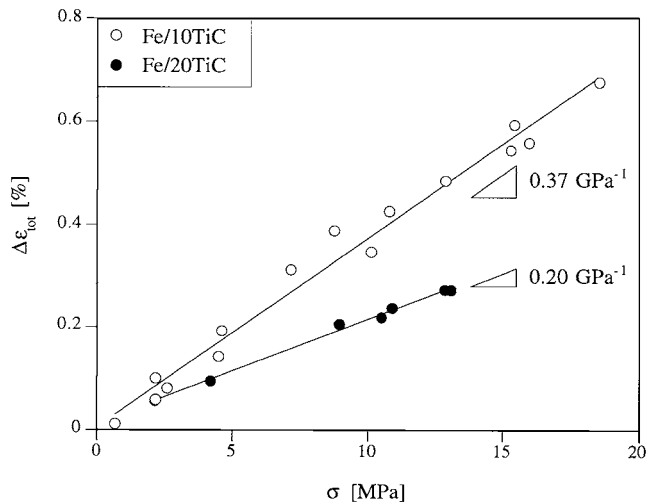


Fig. 9—Strain increment per cycle as a function of the applied stress for Fe/10TiC and Fe/20TiC composites ($T_i = 700$ °C, $T_u = 900$ °C, and $\nu = 6$ to 10 h^{-1}).

crements of $\Delta \epsilon_{\text{tot}} = -0.04$ pct. As shown in Figure 8, the large superplastic strain increments of $\Delta \epsilon_{\text{tot}}/\sigma = 2.2 \text{ GPa}^{-1}$, observed initially upon application of the stress $\sigma = 7 \text{ MPa}$, decrease steadily and stabilize after about 35 cycles to a value of $\Delta \epsilon_{\text{tot}}/\sigma = 1.15 \text{ GPa}^{-1}$. After 140 cycles, the stress was decreased to $\sigma = 1.0$ and 1.5 MPa and negative strain increments of $\Delta \epsilon_{\text{tot}} = -0.05$ and -0.02 pct, respectively, were measured (these strain increments are not shown in Figure 8). After cooling to room temperature, an optical inspection of the sample showed no signs of necking. The

sample was heated again and subjected to the low stresses of $\sigma = 1.1$ and 1.8 MPa , resulting in strain increments of $\Delta \epsilon_{\text{tot}} = -0.07$ and $+0.03$ pct, respectively (not shown in Figure 8). Upon reapplication of the high stress of $\sigma = 4.9 \text{ MPa}$, the same value of $\Delta \epsilon_{\text{tot}}/\sigma = 1.13 \text{ GPa}^{-1}$ was obtained as before the interruption. After about 220 cycles, $\Delta \epsilon_{\text{tot}}/\sigma$ increased again, probably because the onset of necking, visible in Figure 8, leads to locally higher stresses. Low-stress experiments at the end of the experiment again gave negative strain increments of $\Delta \epsilon_{\text{tot}} = -0.2$ to -0.37 pct for stresses of $\sigma \approx 0$ to 0.2 MPa .

C. Thermal Cycling of Fe/TiC Composites

Figure 9 shows, for the composites, the total strain increment as a function of the applied stress for cycles with $T_i = 700$ °C, $T_u = 900$ °C, $\dot{T} = 100$ to 200 K/min , and $\nu = 6$ to 10 h^{-1} . The strain increments for the Fe/10TiC composite ($d(\Delta \epsilon_{\text{tot}})/d\sigma = 0.37 \text{ GPa}^{-1}$) and for the Fe/20TiC composite ($d(\Delta \epsilon_{\text{tot}})/d\sigma = 0.20 \text{ GPa}^{-1}$) are much smaller than for unreinforced iron ($d(\Delta \epsilon_{\text{tot}})/d\sigma = 1.7 \text{ GPa}^{-1}$). As for unreinforced iron, the isothermal deformation was negligible: for a stress of $\sigma = 4.5 \text{ MPa}$ at the upper cycling temperature, Fe/10TiC crept at a rate of $\dot{\epsilon} = 1.8 \cdot 10^{-7} \text{ s}^{-1}$, much lower than the corresponding average cycling strain rate of $d(\Delta \epsilon_{\text{tot}})/dt = 3.2 \cdot 10^{-6} \text{ s}^{-1}$ for $\sigma = 4.6 \text{ MPa}$ and $\nu = 6 \text{ hr}^{-1}$. Under a stress of $\sigma = 4.2 \text{ MPa}$, the Fe/20TiC composite crept isothermally at a rate of $\dot{\epsilon} = 1.0 \cdot 10^{-7} \text{ s}^{-1}$, which was negligible as compared to the average cycling strain rate of $d(\Delta \epsilon_{\text{tot}})/dt = 1.6 \cdot 10^{-6} \text{ s}^{-1}$ for $\nu = 6 \text{ h}^{-1}$.

Figure 10 shows the stress-normalized strain increment $\Delta \epsilon_{\text{tot}}/\sigma$ as a function of the upper-cycle temperature T_u for the Fe/10TiC composite. This figure indicates that the maximum strain increment is obtained at $T_u = 840$ °C and that the contribution of isothermal creep becomes significant above 900 °C.

As shown in Figure 11, the Fe/10TiC sample thermally cycled ($T_i = 700$ °C and $T_u = 880$ °C) under a constant load provided strain data at increasing stresses as the sample cross section diminished; the linear part of Figure 11 was obtained with $\nu = 6$ to 10 h^{-1} and the nonlinear part at a higher cycling frequency of $\nu = 30 \text{ h}^{-1}$. The fracture strain of this Fe/10TiC sample, shown in Figure 11, was $e_f = 231$ pct.

IV. DISCUSSION

A. Thermal Analysis

The DTA curves for unreinforced iron in Figure 2 show peaks at 905 °C on heating (symbol \square) and at 885 °C on

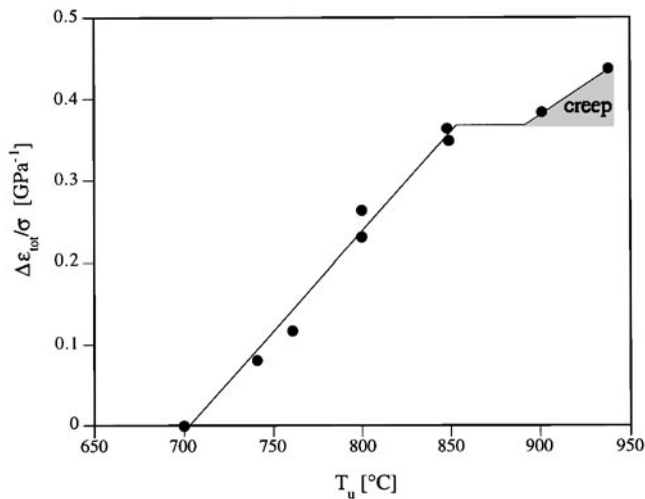


Fig. 10—Stress-normalized strain increment as a function of the upper temperature for Fe/10TiC cycled with constant lower temperature $T_l = 700^\circ\text{C}$ ($\nu = 6\text{ h}^{-1}$ and $\sigma = 14.4$ to 15.6 MPa).

cooling (symbol ■), caused by the α/γ and γ/α transformations which are also visible in the dilatometric curves (Figure 3) as contraction ($\Delta L/L = -0.52\text{ pct}$) upon heating from 840°C to 890°C and as expansion ($\Delta L/L = +0.37\text{ pct}$) upon cooling from 870°C to 845°C . These values are comparable to the linear transformation dilatation reported for pure iron, $\Delta L/L = 0.35$ to 0.38 pct ,^[23,24] and to the allotropic α/γ range for Fe-0.012 wt pct C (814°C to 908°C).^[20] The DTA of iron also reveals peaks 15°C to 20°C below the $\alpha \leftrightarrow \gamma$ temperatures (symbols ▽ and ▼), which may be attributed to a martensitic transformation or to the allotropic transformation occurring over the α/γ range with a recalescence peak (symbol ▼) on cooling. Finally, the DTA curve of iron shows the magnetic transition between 755°C and 765°C on heating (symbol Δ) and cooling (symbol ▲), in good agreement with the Curie temperature of 770°C .^[25]

Except for the magnetic transition, the composites exhibit DTA and dilatometry curves different from those of iron. Upon heating, α/γ peaks (symbol ○, Figure 2) appear around 845°C and 830°C for the 10 and 20 vol pct composites, respectively. These reactions are preceded by large endothermic peaks (symbol ◇) at 735°C within the ferrite region, which correspond to the initial contraction around 700°C found by dilatometry (symbol ◇, Figure 3). Equivalent peaks (symbols ● and ◆) appear upon cooling at significantly lower temperatures (Figures 2 and 3). Figure 3 also shows that the length changes of the composites (which have the same magnitude as those of the iron sample) develop over broad temperature intervals, *i.e.*, between 715°C and 820°C on heating (symbol ○) and between 805°C and 680°C on cooling (symbol ●). The temperatures determined by dilatometry are 15°C to 20°C below those obtained by DTA, probably because the heating rates of $\dot{T} = 10\text{ K/min}$ induced a larger temperature lag in the 1-gram dilatometry sample than in the 0.02-g DTA samples.

Austenite and ferrite can dissolve 660 and 360 ppm equiatomic TiC at 912°C , respectively.^[26] The 300-ppm difference is expected to precipitate and dissolve upon cycling, but corresponds to a volume fraction of 0.05 vol pct, too low to induce significant dilatometric or thermal peaks.

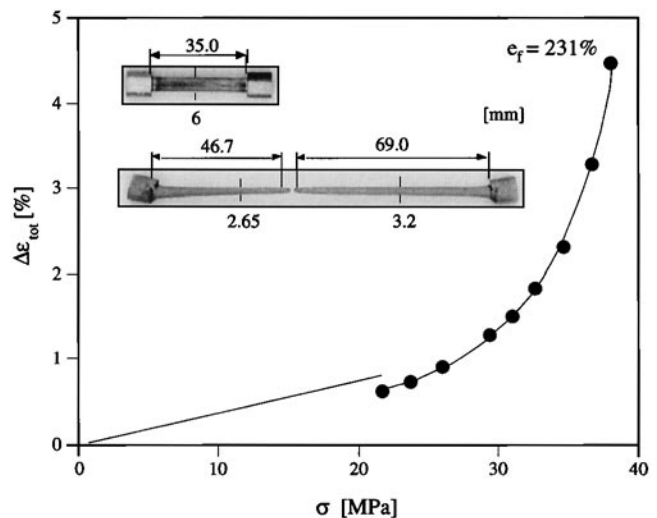


Fig. 11—Total strain increment per cycle as a function of the applied stress for Fe/10TiC deformed until fracture at constant load ($T_l = 730^\circ\text{C}$, $T_u = 880^\circ\text{C}$, and $\nu = 30\text{ h}^{-1}$); the line for $\sigma < 21\text{ MPa}$ is taken from Fig. 9; in the inset are pictures of the sample before and after deformation.

Rather, the composite peaks are attributed to a pearlitic invariant reaction, $\alpha + \text{Fe}_3\text{C} + \text{TiC} \leftrightarrow \alpha + \gamma + \text{TiC}$ (symbols ◇ and ◆), followed by an allotropic transformation, $\alpha + \text{TiC} \leftrightarrow \gamma + \text{TiC}$ (symbols ○ and ●). This interpretation is consistent with the metastable ternary C-Fe-Ti phase diagrams^[27] showing the previous invariant reaction occurring at 740°C , above which a solid solution of carbon and titanium in ferrite transforms continuously to a solid solution of austenite. The higher content of cementite found for the Fe/20TiC composite (Figures 1(f) and (i)) is also expected, based on the higher volume fraction of TiC. The dilatometry results of the composites (Figure 3) are, furthermore, consistent with the temperature-strain curves for Fe-0.2C samples exhibiting a pearlitic reaction, given by Reference 28. Thus, we conclude that the precipitates in Figures 1(e), (f), (h), and (i) are cementite (with, possibly, very small quantities of TiC), as confirmed by their lack of contrast prior to etching, unlike TiC, which is visible without etching.

B. Transformation Superplasticity of Iron

The linear relation given by Eq. [1] can be generalized for the case of a continuous phase transformation.

$$d\left(\frac{\Delta\epsilon}{\sigma}\right) = \frac{5}{6} d\left(\zeta \frac{\Delta V}{V} \frac{1}{\sigma_Y}\right) \quad [2]$$

where $\zeta(T,t)$ is the volume fraction of the new allotropic phase dependent on temperature T and time t , and where the yield stress $\sigma_Y[T, c(T,t)]$ is a function of the temperature T and the carbon concentration $c(T,t)$. Even if one assumes that the phase transformation is limited by heat transfer, rather than transformation kinetics or diffusion, the right-hand side of Eq. [2] depends on the ratio $\zeta(T)/\sigma_Y(T)$, which cannot be evaluated without detailed knowledge of these variables. Instead, Eq. [2] can be approximated by using effective values for the yield stress $\sigma_{Y,\text{eff}}$ and the volume fraction ζ_{eff} .

$$\Delta\varepsilon = \frac{5}{6} \zeta_{\text{eff}} \frac{\Delta V}{V} \frac{\sigma}{\sigma_{y,\text{eff}}} \quad [3]$$

The effective quantities also depend on undercooling, which is itself coupled to cycle characteristics, *e.g.*, temperature amplitudes, heating rates, and heat flux conditions. Since isothermal creep outside the transformation range was negligible, the measured strain increment ($\Delta\varepsilon_{\text{tot}}$) accumulated after a full cycle can be directly compared to the superplastic strain increment ($\Delta\varepsilon$) predicted by Eq. [3]. Because the measured strain increments were identical on heating and on cooling (Figure 5), the stress-normalized superplastic strain increment is $d(\Delta\varepsilon)/d\sigma = d(\Delta\varepsilon_{\text{tot}})/(2d\sigma) = 0.85 \text{ GPa}^{-1}$. With this experimental value for $d(\Delta\varepsilon)/d\sigma$ and the α/γ volume mismatch $\Delta V/V = 3(\Delta L/L) = 1.1 \text{ pct}$,^[23,24] an effective yield stress of $\sigma_{y,\text{eff}} = 10.8 \text{ MPa}$ is obtained from Eq. [3]. While this value fits the low-stress data in Figure 4, the ideal plastic model predicts infinite strain increments when the applied stress reaches the yield value of 10.8 MPa, much below the stresses of about 16 MPa where finite strain increments are still observed. This can be explained if the yield stress increases from a value of 10.8 MPa at low applied stresses to a value of about 16 MPa at large applied stresses due to strain hardening when large strain increments are produced. This hypothesis is supported by the high oxygen content of 0.3 wt pct (originating from the fabrication of the iron powders), which corresponds to a volume fraction of 1.5 vol pct of Fe_3O_4 (or 1.6 vol pct of Fe_2O_3), sufficient for significant dispersion strain hardening.

Both the smaller creep rates observed after cycling, during which the grain size increased by one order of magnitude, and the low-stress exponents measured in isothermal experiments indicate that iron deforms by diffusional creep outside the allotropic range. While pure iron is expected to deform by low-temperature power-law creep with a stress exponent of 6.9 within the stress range of interest,^[29] the observed diffusional creep is attributed to the strengthening effect of carbon and oxide dispersoids, which can lower or, respectively, fully inhibit dislocation creep,^[30] but have little effect on diffusional creep. Also, the change of grain size did not affect the superplastic behavior, which confirms that transformation superplasticity occurs by plastic yield and not by diffusional creep (as is the case for microstructural superplasticity).

The dependence of the transformation superplastic strain ($\Delta\varepsilon$) from the temperature cycle amplitudes within the non-linear regions (Figure 6) can only be described qualitatively based on results obtained from the DTA and dilatometry measurements, since the temperature dependence of the ratio $\zeta(T)/\sigma_y(T)$ is unknown. Dilatometry (Figure 3) indicates that the heating and cooling kinetics of the phase transformation are different, as the $\alpha \rightarrow \gamma$ transformation occurs over a temperature interval ranging from 840 °C to 890 °C, whereas the $\gamma \rightarrow \alpha$ transformation takes place between 870 °C and 845 °C. This 20 °C undercooling for the onset of the $\gamma \rightarrow \alpha$ transformation is consistent with the 20 °C shift in the $\gamma \leftrightarrow \alpha$ DTA peaks (Figure 2). Upon partial cyclic transformation from ferrite to austenite, *i.e.*, variation of the upper cycling temperature, strain increments are expected to appear as soon as the upper cycling temperature exceeds 840 °C and to increase until 890 °C, where $\zeta_{\text{eff}} = 1$ (Figure 6); the increase is probably near-linear with temperature, based on the near-linear dilatometric expansion

and contraction (Figure 3). On cycling from and to the austenite state, a critical temperature amplitude is necessary to induce transformation superplastic strains (Figure 6), similar to observations made in the coefficient of thermal expansion (CTE) mismatch superplasticity of Al-SiC.^[31] This temperature threshold can be explained by two phenomena. First, the $\gamma \rightarrow \alpha$ transformation is undercooled by 20 °C, as discussed previously. Second, because of the high strength of austenite, the initial transformation mismatch can be accommodated elastically, so that ferrite has to form a continuous network before plastic strain can be observed. However, once the temperature threshold (estimated as $\Delta T = 40 \text{ K}$ in Figure 6) is exceeded, a steep increase of the partial transformation strains is expected, according to the $\gamma \rightarrow \alpha$ transformation shown from dilatometry and DTA (Figure 3).

The ratio $d(\Delta\varepsilon_{\text{tot}})/d\sigma = 1.7 \text{ GPa}^{-1}$ measured for iron is significantly smaller than the values of 2.5 to 2.6 GPa^{-1} reported by References (14, 28, and 32), but comparable to the value of 1.5 to 1.7 GPa^{-1} given in Reference 33 (Table III). As shown in Figure 12, there is a strong decrease of $\Delta\varepsilon_{\text{tot}}/\sigma$ (or $d(\Delta\varepsilon_{\text{tot}})/d\sigma$) with increasing carbon concentration, and our data fall within the region where the ratio $\Delta\varepsilon_{\text{tot}}/\sigma$ is very sensitive to the presence of carbon. This is due to the strengthening effect of carbon, which increases the yield stress of the ferrite and, thus, decreases the value of the superplastic strain increment $\Delta\varepsilon$ (Eq. [3]). Also, we find the same strain increments on heating and on cooling (Figure 5), whereas unequal strain increments have been reported in the literature (Table III). This may be due to unequal creep contributions outside the transformation range (ferrite creeps faster than austenite for pure iron), to differences in heating and cooling transformation temperatures (affecting the yield stress), or to different heating and cooling rates (leading to variable ratchetting). The latter mechanism is discussed in more detail subsequently.

Figures 13(a) and (b) show the evolution, with increasing cycle number, of the stress-normalized superplastic strain increment with and without isothermal creep prior to thermal cycling. In the former case, the sample is first loaded until a steady-state creep rate is reached and then thermally cycled. Steady-state strain increments are obtained quickly after about four complete cycles (Figure 13(a)). Since the strain is determined from the total load-train displacement undergoing thermal expansion and contraction during cycling, the convergence behavior in Figure 13(a) reflects the establishment of the dynamic thermal steady state in the sample and the pullrods due to thermal cycling. When the stress was changed during thermal cycling, steady-state increments were obtained after completion of a single cycle. Thus, the establishment of an equilibrium dislocation structure after a change in stress, which is responsible for primary creep, is very rapid upon phase transformation cycling conditions, and primary creep does not contribute significantly to the measured strain, provided the sample was prestrained.

On the other hand, if a sample is first thermally cycled at a small stress to establish thermal equilibrium and then loaded to a high stress without prestraining, steady-state strain increments are obtained only after 35 cycles (Figure 13(b)). This long initial transient is attributed to primary creep, which decreases over time. At steady-state, the stress-normalized strain increment (1.15 GPa^{-1}) is, however, lower than that obtained from Figure 13(a) (1.67 GPa^{-1}). This result is attributed to ratchetting, which in-

Table III. Composition, Stress-Normalized Strain Increment and Elongation to Fracture Found in Literature for Transformation Superplasticity of Iron and Steel

Material*	Carbon (Wt Pct)	Other Elements (Wt Pct)	$\Delta\epsilon_{tot}/\sigma$ or $(d\Delta\epsilon_{tot})/d\sigma$		total (GPa ⁻¹)	Elongation (Pct)	Reference
			heating (GPa ⁻¹)	cooling (GPa ⁻¹)			
Iron	—	—			2.5		(14)
Iron	—	(0.008 N)			2.5		(28)
Iron	0.01	(traces)			1.5		(33)
Iron	0.011	(0.03)			1.7		(33)
Iron	0.012	(0.04)	0.85	0.85	1.7	> 454	present study
Iron	0.02	(0.15) O	1.6	1.0	2.6		(32)
Iron	0.20	—			1.2		(28)
Iron	0.39	—			0.70		(14)
Steel	0.012	0.30	0.16	0.26	0.42		(40)
Steel	0.03	0.49	0.19	0.13	0.32	92	(16)
Steel SS41	0.15	0.46	0.19	0.09	0.28		(39)
Steel SS41	0.15	0.53	—	0.10	0.46		(40)
Steel S15CK	0.16	1.06	heat > cool		0.45	> 500	(17)
Steel AISI 1018	0.18	0.84	0.13	0.11	0.24	515	(15)
Steel	0.20	—			0.41		(38)
Steel S20C	0.21	0.58	0.17	0.17	0.34		(39)
Steel	0.23	0.49			0.70		(28)
Steel AISI 1045	0.40	0.97	0.13	0.11	0.24	500	(15)
Steel	0.82	1.13			0.15		(37)
Steel SK5	0.90	0.77		0.08			(40)
Steel AISI 1095	0.98	0.58	0.13	0.11	0.24	580	(15)
Steel AISI 52100	1.07	2.17	0.12	0.09	0.21	720	(15)

*Labeled "Iron," if no significant alloying elements other than carbon are present, "Steel" otherwise; except Ref. 38.

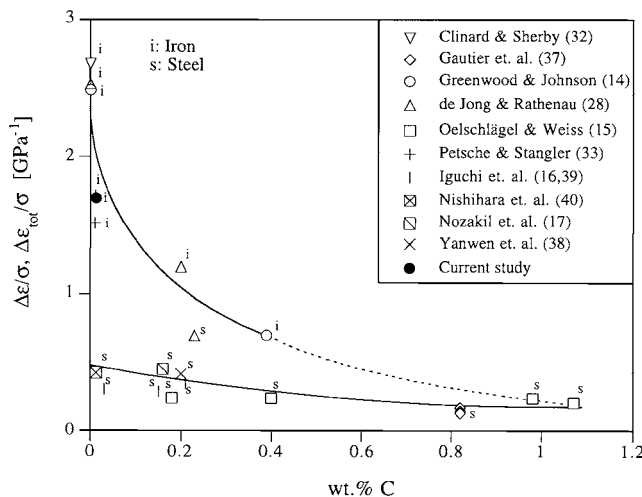


Fig. 12—Effect of the carbon content of iron and steel on the stress-normalized total strain per cycle (Table III).

duces plastic deformation under no or little applied stress as a result of a macroscopic strain gradient traveling through the sample, due to a sharp phase front produced by a steep temperature gradient.^[34] In the case of iron, where the stronger phase (γ Fe) is denser than the weaker phase (α Fe), ratchetting causes a contraction perpendicular to the propagation direction of the phase front,^[34] *i.e.*, in the axial direction of the radially heated samples.

The presence of ratchetting was confirmed by the following experiments. When a thin, 1.6-mm-diameter grounded K-type thermocouple with a fast response was used to control the sample surface temperature, no ratchetting was ob-

served since the stress-normalized strain increment $\Delta\epsilon_{tot}/\sigma = 1.67$ GPa⁻¹ (Figure 13(a)) was identical to the differential slope $(d\Delta\epsilon_{tot})/d\sigma = 1.7$ GPa⁻¹ (Figure 4). In this case, the macroscopic phase front is diffuse, as the surface temperature measured by the thermocouple accurately reflects the sample temperature. However, when a thick, 3.2-mm-diameter ungrounded R-type thermocouple was used to control the surface temperature, a much higher heat flux was delivered by the furnaces due to the slow response of the thermocouple, leading to a sharper transformation front. As expected, ratchetting was then observed as a decrease of the stress-normalized strain increments $\Delta\epsilon_{tot}/\sigma = 1.2$ GPa⁻¹ (Figure 13(b)) after 35 cycles.

The average ratchetting strain ($\Delta\epsilon_{tot,0}$) can be estimated from the difference between the slope in Figure 4 ($(d\Delta\epsilon_{tot})/d\sigma = 1.7$ GPa⁻¹) and the previous stress-normalized strain increments ($\Delta\epsilon_{tot}/\sigma$).

$$\Delta\epsilon_{tot,0} = \left(\frac{d(\Delta\epsilon_{tot})}{d\sigma} - \frac{\Delta\epsilon_{tot}}{\sigma} \right) \sigma \quad [4]$$

With $\sigma = 7.2$ MPa (Figure 13(b)), Eq. [4] gives $\Delta\epsilon_{tot,0} = 0.40$ pct; with $\Delta\epsilon_{tot}/\sigma = 1.13$ at $\sigma = 4.9$ MPa (Figure 8), $\Delta\epsilon_{tot,0} = 0.28$ pct is obtained. Considering the case of a phase transformation front traveling radially in a cylindrical specimen consisting of a rigid phase and a perfectly plastic phase with low yield stress, an estimate for the ratchetting strain is $\Delta\epsilon_{tot,0} = (2/3)|\Delta V/V| = 0.70$ pct for a full cycle encompassing two allotropic transformations. This estimate is reasonably close to the values obtained from Eq. [4] and the low-stress measurements giving $\Delta\epsilon_{tot} = -0.2$ to -0.37 pct.

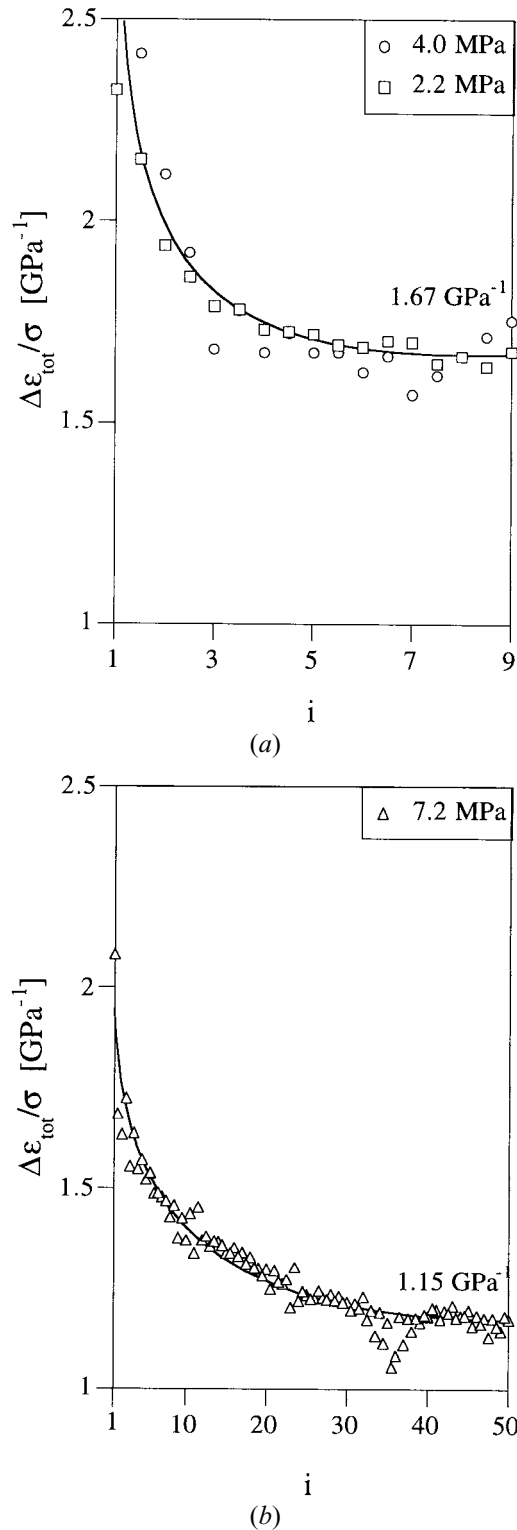


Fig. 13—Convergence behavior of the stress-normalized strain increments as a function of the number of cycles for iron: (a) with isothermal creep prior to thermal cycling and with a fast response thermocouple; and (b) without isothermal creep prior to thermal cycling (promoting primary creep) and with a slow-response thermocouple (promoting ratchetting).

Finally, ratchetting is not constant in the long-term experiment (Figure 8), where the magnitude of the measured negative ratchetting strains was significantly larger at the end of the experiment. A possible explanation is that the

decreased cross-sectional area increased the net energy flux from the furnace and, thus, sharpened the transformation front. As for the decreasing primary creep contribution, this effect results in a continuously decreasing value of $\Delta\epsilon_{\text{tot}}/\sigma$.

C. Transformation Superplasticity of Fe/TiC Composites

In contrast to titanium containing 10 vol pct TiC particles, which exhibited a significantly higher value of $d(\Delta\epsilon_{\text{tot}})/d\sigma$ as compared to unreinforced titanium,^[18] the iron-based composites in the present investigation display values of $d(\Delta\epsilon_{\text{tot}})/d\sigma$ substantially lower than the unreinforced matrix. This discrepancy can be explained by two major differences existing between these systems. First, the titanium composites relaxed internal allotropic stresses by power-law creep. Unlike time-independent plasticity by yield for the present iron-based composites, the creep strain rate of the titanium system is very stress sensitive, so that stress concentrations due to a mismatch between the elastic reinforcement and the transforming matrix induce large strains. Second, it is apparent from the metallographic sections (Figures 1(d) through (i)) and the thermal analysis (Figures 2 and 3) that the matrices of the composites are different from the unreinforced iron sample and from each other, due to the slight solubility of TiC in iron, increasing both the substitutional (Ti) and interstitial (C) content in the matrix and leading to cementite precipitation below 740 °C, as discussed earlier. As shown in Figure 12, both substitutional alloying elements and carbon result in lowered superplastic strains. The slight dissolution of TiC into iron, thus, leads to a matrix with a substantially higher intrinsic strength and lower transformation temperatures, so that the compositional differences between the three types of samples overwhelm any effects due to reinforcement volume fraction.

In allotropic composites, two additional sources of mismatch between the matrix and reinforcement exist if the interface between the reinforcement and the matrix is well bonded, as in Fe/TiC, where the reinforcement shows some solubility in the matrix (but unlike an insoluble, weakly bonded system such as Fe/Al₂O₃, where interface fracture occurs upon phase transformation^[35]). First, if the two phases have different CTEs, thermal mismatch stresses occur during a thermal excursion of ΔT , which can lead to superplastic strain increments as observed in Al/SiC composites upon repeated thermal cycling.^[36] Second, if the matrix is allotropic, its transformation in the presence of nontransforming particulates also induces mismatch stresses and a corresponding superplastic strain increment, as recently observed in the Ti/TiC system.^[18] Assuming that these contributions occur independently, an effective mismatch $(V/V)_{\text{eff}}$ can be defined with the rule of mixture.

$$\left(\frac{\Delta V}{V}\right)_{\text{eff}} = (1 - f) \left|\frac{\Delta V}{V}\right| + f \left|\frac{\Delta V}{V} + 3\Delta\alpha\Delta T\right| \quad [5]$$

where f is the volume fraction of reinforcement and $\Delta\alpha$ is the difference between the reinforcement CTE and the average matrix CTE (all CTEs are assumed isotropic) over the temperature interval ΔT . In Eq. [5], the first term, $(1 -$

$f)|\Delta V/V|$, is the transformation mismatch within the matrix, and the second term, $f|\Delta V/V + 3\Delta\alpha\Delta T|$, is the composite mismatch between the matrix and the reinforcement, consisting of both transformation and thermal expansion.

In the Fe/TiC system, the thermal and allotropic mismatch strains have opposite signs, *i.e.*, on heating, the thermal expansion mismatch between iron and TiC partially offsets the contraction due to the α/γ phase transformation of iron. Neglecting the small thermal expansion mismatch outside the transformation range (which is assumed to be elastically accommodated), we consider only the mismatch within the interval $\Delta T = +130$ K, where the phase transformation (including the pearlitic reaction) occurs for the composites (Figure 3). We take for TiC a CTE value of $\alpha = 8.0 \cdot 10^{-6} \text{ K}^{-1}$; [22] for the matrix, an average of the CTE for ferrite, $\alpha = 16.6 \cdot 10^{-6} \text{ K}^{-1}$; [24] and for austenite, $\alpha = 23.3 \cdot 10^{-6} \text{ K}^{-1}$. [24] With a maximum thermal mismatch of $3\Delta\alpha\Delta T = +0.47$ pct and an allotropic mismatch of $\Delta V/V = -1.1$ pct, [23,24] the effective mismatch given by Eq. [5] reduces, for the present case, to $|\Delta V/V + 3f\Delta\alpha\Delta T| = 1.05$ pct for Fe/10TiC and to $|\Delta V/V + 3f\Delta\alpha\Delta T| = 1.01$ for Fe/20TiC. Effective yield stresses of 47 and 84 MPa, respectively, are then calculated from Eq. [3] for the ferritic matrices of the composites. While these values are much higher than for the unreinforced iron specimen, they are within a physically plausible range. They cannot, however, be directly compared to a yield stress experimentally determined by tensile testing, as they correspond to an average over the transformation range of the yield stress, as discussed earlier. Introducing the previous effective yield stress values and the allotropic matrix mismatch of $|\Delta V/V| = 1.1$ pct from Eq. [3], we get $d(2\Delta\epsilon)/d\sigma = 0.39$ and 0.22 GPa^{-1} for the unreinforced matrices, which is within the range of values observed in Figure 12 for carbon-containing alloyed steel.

Finally, the Fe/10TiC fracture experiment demonstrates that superplastic strains ($\epsilon_f = 231$ pct, Figure 11) can be reached in tension in these composites, despite their room-temperature brittleness and hardness. The experiment also illustrates that rapid strain rates can be obtained: for a strain increment of 2.4 pct per cycle (applied stress of 35 MPa, Figure 11) and a cycling frequency of 30 h^{-1} , the measured average strain rate of $d(\Delta\epsilon_{\text{tot}})/dt = 2 \cdot 10^{-4} \text{ s}^{-1}$ is well within the range used for commercial superplastic forming.

V. CONCLUSIONS

Transformation superplasticity was studied in iron samples subjected to temperature cycling through the α/γ phase field with a superimposed external uniaxial stress.

1. Within the stress range of interest, deformation by steady-state creep is insignificant as compared to transformation superplastic deformation. If the material is not crept prior to cycling, primary creep can, however, contribute to the measured transformation superplastic strains, but this contribution diminishes with time. Also, thermal ratchetting is observed under high-heat flux conditions where a sharp transformation front is created; the observed contraction of 0.3 pct is in agreement with existing ratchetting models.
2. When ratchetting and primary creep are eliminated,

equal strain contributions result from the α/γ and γ/α transformations. The strain per cycle is linearly proportional to the applied stress ($\Delta\epsilon_{\text{tot}}/\sigma = 1.7 \text{ GPa}^{-1}$) for stresses up to 6 MPa, but increases nonlinearly for higher stresses.

3. By considering effective quantities for the yield stress and the volume mismatch, the yield model of Greenwood and Johnson [14] can be adapted to describe the present case of a phase transformation through a two-phase field where the preceding properties are temperature and/or concentration dependent. The effective yield stress determined within the linear range (10.8 MPa) is significantly smaller than the effective yield stress deduced from the nonlinear divergence (16 MPa). This is attributed to strain hardening caused by dissolved carbon and iron-oxide dispersoids.
4. Upon partial cycling from the austenite field, superplastic strains are initially smaller than upon partial cycling from the ferrite field. This behavior is explained by undercooling of the transformation and by elastic accommodation of mismatch stresses in the strong austenite.

Transformation superplasticity was investigated in iron-matrix composites containing 10 and 20 vol pct TiC particulates.

1. Superplastic behavior was demonstrated for the Fe/10TiC composite, which showed a total tensile fracture strain of 231 pct which was, however, smaller than the strain of 454 pct achieved without failure in unreinforced iron. Average strain rates of $2 \cdot 10^{-4} \text{ s}^{-1}$ can be achieved in that composite, comparable to those used in commercial superplastic operations.
2. The composites show transformation superplastic strain increments ($\Delta\epsilon_{\text{tot}}/\sigma = 0.37 \text{ GPa}^{-1}$ for Fe/10TiC and $\Delta\epsilon_{\text{tot}}/\sigma = 0.20 \text{ GPa}^{-1}$ for Fe/20TiC), which are lower than those of unreinforced iron. This is attributed to the slight dissolution of TiC in the matrix, which increases its yield strength by solid-solution strengthening and by reducing the transformation temperature range (as also observed by dilatometry and calorimetry).
3. The yield model of Greenwood and Johnson [14] predicts effective matrix yield stresses of 47 MPa for Fe/10TiC and 84 MPa for Fe/20TiC. The composite superplastic strains are comparable to literature data for unreinforced steels, which also show decreasing transformation superplastic strains with increasing carbon content.
4. Calorimetry and dilatometry show that the α/γ allotropic transformation followed by cementite precipitation occurs over a broad temperature interval of 130 °C. Strains produced by partial transformation through this phase field increase linearly with the temperature excursion, in agreement with the expected mismatch evolution determined by dilatometry.

ACKNOWLEDGMENTS

This study was supported by the United States Army Research Office under Grant No. DAAH04-95-1-0629, monitored by Dr. W.C. Simmons.

REFERENCES

1. C. Raghunath, M.S. Bhat, and P.K. Rohatgi: *Scripta Metall.*, 1995, vol. 32, pp. 577-82.
2. Ö.N. Dogan and J.A. Hawk: *Scripta Metall.*, 1995, vol. 33, pp. 953-58.
3. T.Z. Kattamis and T. Sukanuma: *Mater. Sci. Eng.*, 1990, vol. A128, pp. 241-52.
4. B.S. Terry and O.S. Chinyamakobvu: *J. Mat. Sci. Letters*, 1991, vol. 10, pp. 628-29.
5. A. Saïdi, A. Chrysanthou, J.V. Wood, and J.L.F. Kellie: *J. Mat. Sci.*, 1994, vol. 29, pp. 4993-98.
6. C. Jouanny-Tresy, M. Vardavoulias, and M. Jeandin: *JOM* 1995, vol. 47, Nr. 4, pp. 26-30.
7. J.W. Edington, K.N. Melton, and C.P. Cutler: *Progr. Mater. Sci.*, 1976, vol. 21, pp. 61-158.
8. T.G. Nieh, J. Wadsworth, and O.D. Sherby: *Superplasticity in Metals and Ceramics*, Cambridge University Press, Cambridge, UK, 1997.
9. E. Scheil: *Z. Anorg. Org. Chem.*, 1932, vol. 207, pp. 21-40.
10. L.F. Porter and P.C. Rosenthal: *Acta Metall.*, 1959, vol. 7, pp. 504-14.
11. R.G. Stringfellow, D.M. Parks, and G.B. Olson: *Acta Metall. Mater.*, 1992, vol. 40, pp. 1703-16.
12. J.M. Diani, H. Sabar, and M. Berveiller: *Int. J. Eng. Sci.*, 1995, vol. 33, pp. 1921-34.
13. G.B. Olson: *J. Phys. IV*, 1996, vol. 6, pp. C1-407-418.
14. G.W. Greenwood and R.H. Johnson: *Proc. R. Soc. London*, 1965, pp. 403-22.
15. D. Oelschlägel and V. Weiss: *Trans. ASM*, 1966, vol. 59, pp. 143-54.
16. N. Iguchi, Y. Oka, and Y. Saotome: *J. Jpn. Inst. Met.*, 1974, vol. 38, pp. 725-30.
17. H. Nozaki, Y. Uesugi, Y. Nishikawa, and I. Tamura: *J. Jpn. Inst. Met.*, 1985, vol. 49, pp. 260-66.
18. D.C. Dunand and C.M. Bedell: *Acta Metall. Mater.*, 1996, vol. 44, pp. 1063-76.
19. D.C. Dunand and S. Myojin: *J. Mater. Sci. Eng.*, 1997, vol. 230, pp. 25-32.
20. *ASM Handbook: Alloy Phase Diagrams*, ASM, Metals Park, OH, 1992, pp. 2.110-2.114.
21. *Handbook of Chemistry and Physics*, D.R. Lide, ed., CRC Press, Boca Raton, FL, 1995, pp. 4.63-12.172.
22. *Thermophysical Properties of High Temperature Materials*, Y.S. Touloukian, ed., The McMillan Company, New York, NY, 1967, vol. 5, pp. 176-87.
23. Z.S. Basinski, W. Hume-Rothery, and A.L. Sutton: *Proc. R. Soc. London*, 1955, vol. 229, pp. 459-67.
24. *Thermophysical Properties of Matter*, Y.S. Touloukian, R.K. Kirby, R.E. Taylor, and P.D. Desai, eds., IFI/Plenum, New York, NY, 1975, vol. 12, p. 157.
25. *Metals Handbook: Properties and Selection: Iron, Steels and High Performance Alloys*, ASM, Metals Park, OH, 1990, p. 132.
26. A.K. Taylor: *Scripta Metall.*, 1995, vol. 32, pp. 7-12.
27. *Handbook of Ternary Alloy Phase Diagrams*, P. Villars, A. Prince, and H. Okamoto, eds., ASM International, Materials Park, OH, 1995, p. 6838.
28. M. de Jong and G.W. Rathenau: *Acta Metall.*, 1959, vol. 7, pp. 246-53.
29. H.J. Frost and M.F. Ashby: *Deformation-Mechanism Maps: The Plasticity and Creep of Metals and Ceramics*, Pergamon Press, New York, NY, 1982, pp. 60-68.
30. E. Arzt: *Res. Mechanica*, 1991, vol. 31, pp. 399-453.
31. S.M. Pickard and B. Derby: *Acta Metall.*, 1990, vol. 38, pp. 2537-52.
32. F.W. Clinard and O.D. Sherby: *Acta Metall.*, 1964, vol. 12, pp. 911-19.
33. S. Petsche and F. Stangler: *Z. Metallkd.*, 1971, vol. 62, pp. 601-05.
34. J.J. Stobo: *J. Nucl. Mater.*, 1960, vol. 2, pp. 97-109.
35. J. Bendixen and A. Mortensen: *Scripta Metall.*, 1991, vol. 25, pp. 1917-20.
36. D.C. Dunand and B. Derby; in *Fundamentals of Metal Matrix Composites*, S. Suresh, A. Mortensen, and A. Needleman, eds., Butterworth-Heinemann, Boston, MA, 1993, pp. 191-214.
37. E. Gautier and A. Simon: *Phase Transformations '87*, University of Cambridge, Cambridge, United Kingdom, 1987, G.W. Lorimer, ed., Institute of Metals, London, 1987, pp. 285-87.
38. W. Yanwen, F. Zezhou, and S. Shangchen: *Superplasticity and Superplastic Forming*, C.G. Hamilton and N.E. Paton, eds., MRS, Pittsburgh, PA, 1988, pp. 562-67.
39. N. Iguchi, Y. Oka, and Y. Saotome: *J. Jpn. Inst. Met.*, 1975, vol. 39, pp. 357-61.
40. T. Nishihara, K. Asami, and N. Iguchi: *J. Jpn. Inst. Met.*, 1977, vol. 41, pp. 188-93.